Trans. Japan Soc. Aero. Space Sci.
Vol. 51, No. 172, pp. 86–92, 2008

# Numerical Study and Performance Prediction for Gaseous Hydrogen/Oxygen Bell Nozzle*

By Nobuyuki TSUBOI,[1)] Takashi ITO[2)] and Hiroshi MIYAJIMA[2)]

[1)]*Institute of Space and Astronautical Science, Japan Aerospace Exploration Agency, Sagamihara, Japan*
[2)]*Institute of Aerospace Technology, Japan Aerospace Exploration Agency, Kakuda, Japan*

(Received April 9th, 2007)

Three-dimensional reactive full Navier-Stokes simulations of hydrogen/oxygen flow in a nozzle with area ratio of 140 are evaluated using a detailed chemical kinetics reaction model. The flows over each overlapped grid are computed using a unified zonal method technique. The flow field computed by the present CFD code shows good agreement with the flow field computed by the TDK code except the position of the weak compression wave focusing on the nozzle axis. $I_{sp}$ profiles of the subscale nozzle computed by the CFD code assuming a laminar condition agree well with the experiment and those calculated by the TDK code. The measured heat flux distributions at higher nozzle expansion ratios also agree well with the laminar CFD results. The inconsistency of the prediction of turbulent boundary layer loss between TDK and CFD leads to some difference in $I_{sp}$. The effect of grid resolution on $I_{sp}$ turned out to be small in the present conditions.

**Key Words:** Propulsion, Rocket Nozzle, Computational Fluid Dynamics, Specific Impulse

## 1. Introduction

Recent heavy-lift Japanese launchers and reusable launch vehicles now under development mainly use liquid fuel and liquid oxidizer to power the vehicle to orbit. The selection of the propellant combination will be a compromise of various factors, such as economic factors, performance of propellants, purpose of mission, etc. The major propellant combination used in Japan is liquid hydrogen and liquid oxygen. Although a rocket engine that uses LNG and LOX as propellants is now under development, $LH_2$ and LOX are likely to be used for most advanced propulsion systems, such as air-breathing engines and SCRAM jet engines, and such propellants are already being used for firing tests. The major reason forusing $LH_2$ is that it gives the highest specific impulse for a non-toxic combination, which makes it best for high-vehicle-velocity missions.

There are some computational codes for predicting thrust performance of liquid-fuel engines. Gordon and McBride presented a computational code that computes a quasi one-dimensional inviscid flow with a chemical equilibrium and frozen state.[1)] The performance, such as thrust, specific impulse ($I_{sp}$), pressure, etc., as a function of nozzle area ratio can be obtained using this code. The program is now used by many organizations and companies and is open for public use. Nakahashi et al. developed the TDK code (Two-dimensional Kinetic Flow code),[2)] which uses Gordon and McBride's code as a starting point. The TDK code solves the Euler equations for the supersonic expansion flow by using a space-marching method and the boundary layer effect is estimated by solving the boundary layer integral equations. The TDK code solves chemical non-equilibrium flow in a very short computation time and obtains the rocket nozzle performance, such as thrust coefficient and specific impulse. While this code can sufficiently estimate the effect of chemical non-equilibrium characteristics on nozzle performance, which largely depend on the chamber pressure, there are slight differences between the TDK and experiment for the dependency of mixture ratio and wall temperature on nozzle performance. These discussions, which are based on TDK results, assume non-separating and non-injected flow in a nozzle. An expander bleed cycle, which injects part of the unburned hydrogen gas inside the nozzle, is being used for Japan's 2nd stage engine with a highly expanding nozzle. Therefore, TDK cannot accurately predict the effects of the interactions between the main flow and the secondary flow on the nozzle performance. It also cannot predict the cooling effects of injection of the secondary flow.

NASA, ESA, and other aerospace industries have been developing performance prediction tools by using the CFD technique. Wang et al.[3–5)] carried out two-dimensional and three-dimensional simulations for the Space Shuttle Main Engine (SSME) to estimate the performance, such as $I_{sp}$ and heat flux on the nozzle wall. Their results agreed well with the experimental data. Hagemann et al.[6)] studied the effects of film cooling and turbulence models in the Vulcain nozzle. Yang[7)] studied these effects using a subscale nozzle. Haidinger[8)] investigated the effects of turbulence models on $I_{sp}$ for adiabatic and cooled walls for a clean nozzle and also for a film cooled nozzle. Takahashi et al.[9)] and Shimizu et al.[10)] carried out CFD computations to investigate the effect of side loads during start-up and shut-down transients.

© 2008 The Japan Society for Aeronautical and Space Sciences

*Translated from Journal of The Japan Society for Aeronautical and Space Sciences, Vol. 54, No. 633, 2006, pp. 441–447

Recent studies focus on the effects of film cooling, side loads, and turbulence models on nozzle performance, but studies focused on thrust performance itself have not been carried out except using TDK.

The main objective of the present study is to validate the CFD code by comparing the results obtained by the TDK code and experiments. The CFD code has fewer assumptions than the TDK code and the computation is performed using the non-film-cooled, subscale and full-scale, 10-ton thrust, bell-type rocket nozzle. Furthermore, the computed $I_{sp}$ performance and grid dependency are evaluated along with comparison of wall pressure and wall heat flux between the numerical simulations and experiments.

## 2. Numerical Method

The governing equations are three-dimensional compressible Navier-Stokes equations with conservative equations for multi-species. The chemical species includes nine species such as $H_2$, $O_2$, O, H, OH, $HO_2$, $H_2O_2$, $H_2O$, and $N_2$. Although it is not necessary to consider all the above chemical species to solve the present reactive nozzle flow, the present code was developed for extension to future applications, such as supersonic combustion in a SCRAM jet and detonation flows.

The stiffness problem arises when solving these supersonic reactive flows numerically because the characteristic reaction time is significantly smaller than the characteristic fluid flow time. Therefore, a linearly point implicit technique is used to solve the source term including the chemical reaction and a LU-ADI factorization algorithm[11] is used for integration in time.

The convective terms are obtained by AUSM-DV[12] and second-order space accuracy is evaluated using MUSCL with a minmod function.[13] The viscous terms are calculated by central differencing. The Petersen and Hanson model[14] including 9 species and 18 elementary reactions is used to calculate chemical reaction. This reaction model was proposed for computing detonation and supersonic combustion flow achieving local pressures higher than 100 atm. The validation for applying such a reaction model to these kinds of flow fields is presented elsewhere.[15] It can be assumed that the present reaction model is sufficiently reliable for application to the present rocket nozzle flow computation. The present chemical reaction assumes chemical non-equilibrium. This computational code can compute the flow field that uses overset grids by using the Fortified Solution Method (FSA),[16] however, it is not used here because a single grid is used. This method can be applied to reactive flow with minor modification. The eddy viscosity is evaluated using the Baldwin-Lomax turbulence model.[17] However, the effect of the turbulence model and law of the wall (which is the boundary condition for some turbulence models) on heat flux is not well discussed. Since the present computation assumes no-flow separation, the Baldwin-Lomax model, which does not use the law of the wall for the wall boundary condition, is used. For subscale nozzle flow, a laminarization phenomena in the boundary layer has been reported.[18–21] Therefore, it is preferable to use Large Eddy Simulation (LES) to predict the transition and inverse-transition between turbulent and laminar flow. The quantitative discussions of the effect of the turbulence model are left for future studies.

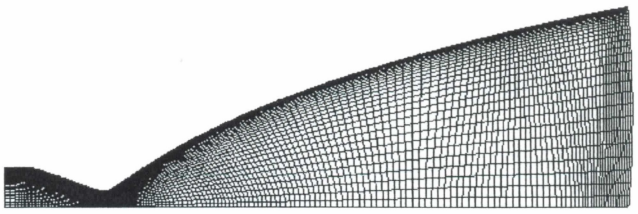

Fig. 1. Computational grids for CFD.

The isothermal, non-slip, and non-catalytic conditions are applied for the wall boundary conditions. For the condition inside the combustion chamber, the mixture ratio ($O/F$) is set to 4.5, 5.5, and 6.5, the stagnation pressure ($p_0$) is set to 33.88 atm, and the stagnation temperature ($T_0$) is set to 3152, 3374, and 3485 K.[22] The temperature inside the combustion chamber was obtained using the combustion pressure, the enthalpies of LOX and gaseous hydrogen supplied to the combustion chamber, and the mixture ratio inside the chamber, assuming that the combustion chamber is in chemical equilibrium.[1,2] The chemical mass fractions obtained from the chemical equilibrium computation are also used for the inlet conditions. The combustion efficiency is assumed to be 100% at the inlet for both subscale and fullscale nozzle simulations. The upstream inflow boundary is shown to be the left surface in Fig. 1, where the boundary layer thickness is assumed to be zero and the uniform flow is given at the boundary. For the inlet boundary conditions, the total enthalpy and individual chemical species are fixed, the axial velocity is extrapolated, and the radial velocity is set to zero.[23] The temperature is obtained from the total enthalpy and velocities, and the pressure and density are obtained assuming an isentropic state. The throat diameter ($D^*$) for the subscale nozzle is 28 mm and the detailed geometries of the nozzle are described elsewhere.[22] The throat Reynolds number $Re_{D^*}$ obtained from the viscosity, density, and velocity at the throat is $4.7 \times 10^5$ under $O/F = 5.5$. The nozzle expansion ratio is 140. The fullscale nozzle has $D^* = 136$ mm[24] for throat diameter and the throat Reynolds number is $Re_{D^*} = 2.2 \times 10^6$. For subscale nozzle flow, the boundary layer is found to be in its transition region.[25] The wall temperatures are uniformly distributed as 300 K and 800 K for the subscale nozzle and 800 K for the fullscale nozzle, respectively. The heat flux comparisons with the experiment for the subscale nozzle are performed using the 300 K constant wall temperature condition and other comparisons such as nozzle performance are carried out using the 800 K constant wall temperature condition. The computational grid system is shown in Fig. 1 and the grid points are $202 \times 9 \times 77$. Although the present flow field is axisymmetric, the computational grid is distributed in the circumferential direction for future studies, such as side-force anal-

Table 1. Simulation conditions.

| Item | Subscale | Fullscale |
|---|---|---|
| Chamber pressure, atm | 33.88 | ← |
| Chamber temperature, K | 3152, 3374, 3485 | ← |
| Mixture ratio ($O/F$) | 4.5, 5.5, 6.5 | ← |
| Throat diameter $D^*$, mm | 28 | 136 |
| Throat Reynolds number $Re_{D^*}$ ($O/F = 5.5$) | $4.7 \times 10^5$ | $2.2 \times 10^6$ |
| Wall temperature $T_w$, K | 300, 800 | 800 |
| Grid points | $202 \times 9 \times 77$ | $277 \times 9 \times 131$ |
| Minimum grid size near wall, μm | 0.1 | ← |
| Laminar/Turbulent | Laminar<br>Turbulent | <br>Turbulent |

ysis due to non-symmetric flow separation and film cooling analysis, assuming introduction of the film coolant inside the nozzle flow. For quantitative discussions of heat flux distributions, the minimum grid size near the wall surface is set to 0.1 μm although the $I_{sp}$ performance is insensitive to the grid resolution near the wall. The $277 \times 9 \times 131$ grid points are distributed for the fullscale nozzle and the same grid size as the subscale nozzle (0.1 μm) is applied near the nozzle surface. All the above parameters are summarized in Table 1.

The non-reactive flow is initially computed using a local time-stepping procedure until the flow becomes steady state. The reactive flow is then simulated using a global time-stepping procedure. The maximum value of CFL number is 1000.

## 3. Results and Discussions

First, the comparisons of TDK, experiments, and CFD for the subscale nozzle are presented. Then, comparisons of TDK and CFD for the fullscale nozzle are discussed. Finally, the effects of grid resolution on nozzle performance are evaluated.

### 3.1. Results of subscale nozzle

CFD results are presented in Fig. 2 (top). TDK results in the supersonic section are shown in Fig. 2 (bottom). Although there is a small discrepancy at the weak compression wave focus, the overall flow structure agrees well between the two results. The pressure distributions on the nozzle surface for CFD, TDK, and the experiments are plotted in Fig. 3. All three results agree well and no difference between laminar and turbulent flow occurs in the CFD results. Therefore, we cannot determine whether the boundary layer along the wall is laminar or turbulent from the experimental wall static pressure data. Figures 4–7 compare the CFD and TDK results on the symmetry axis. A turbulent boundary layer is considered in the CFD computations. The CFD and TDK results agree well except where the compression wave focuses on the symmetry axis in Fig. 4. The Mach number and temperature distributions also agree well between as shown in Fig. 5. Figures 6 and 7 show the axial

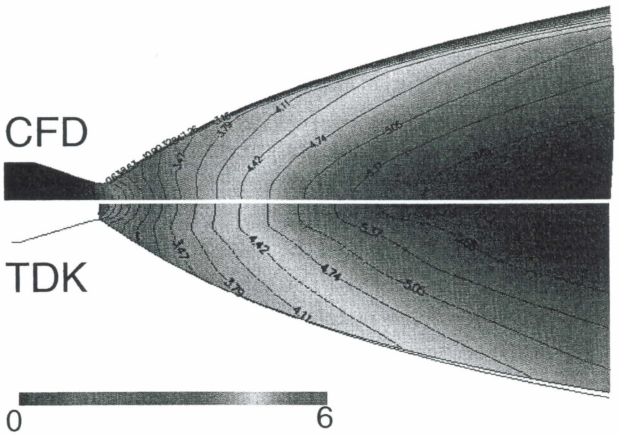


Fig. 2. Comparison of Mach contours in subscale nozzle between TDK and CFD ($O/F = 5.5$, $T_w = 800$ K).

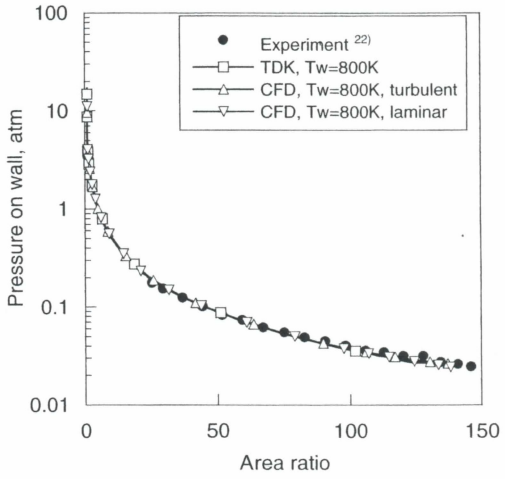


Fig. 3. Comparison of surface pressure in subscale nozzle ($O/F = 5.5$, $T_w = 800$ K).

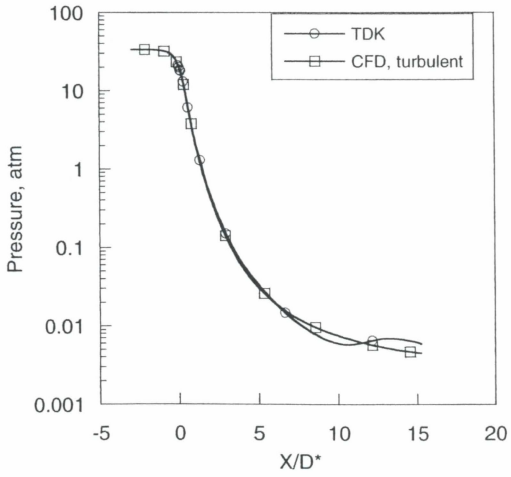


Fig. 4. Comparison of pressure along symmetric axis in subscale nozzle ($O/F = 5.5$, $T_w = 800$ K).

mass fraction of each chemical species. The vertical axis is enlarged in this figure. Although a different chemical reaction model is used for CFD and TDK, the plots are very similar. A similar trend is reported in the computed results

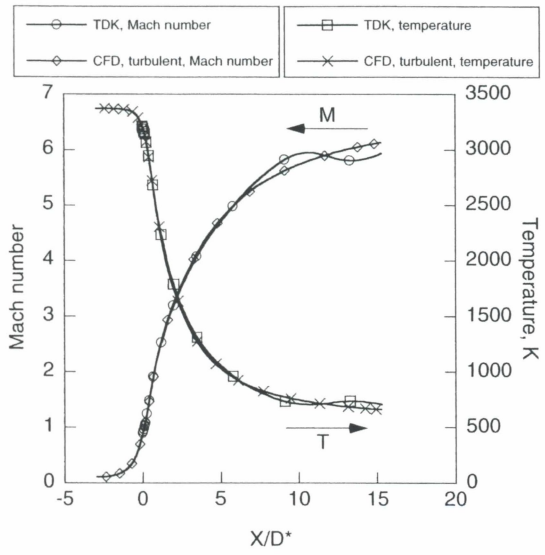


Fig. 5. Comparison of Mach number and temperature along symmetric axis in subscale nozzle ($O/F = 5.5$, $T_w = 800$ K).

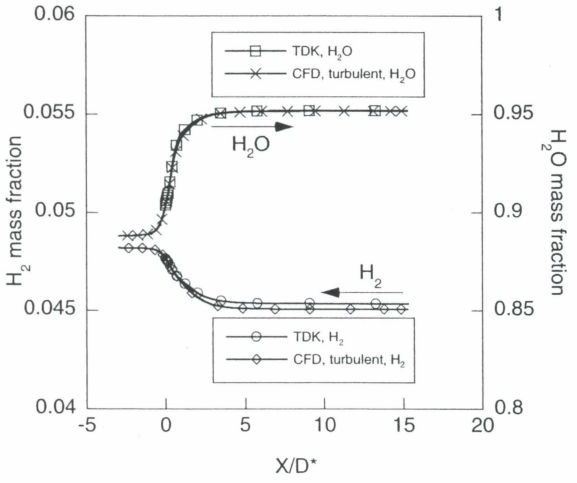


Fig. 6. Comparison of $H_2$ and $H_2O$ mass fractions along symmetric axis in subscale nozzle ($O/F = 5.5$, $T_w = 800$ K).

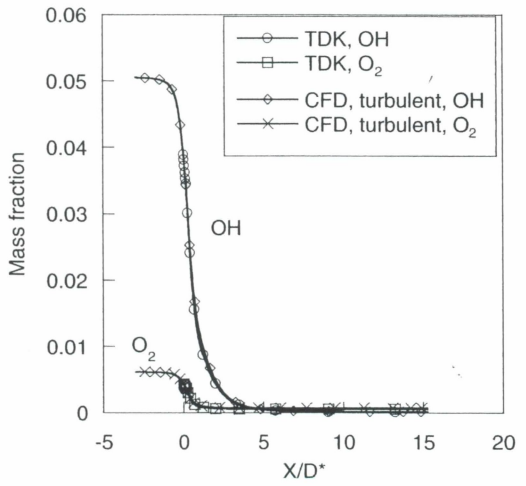


Fig. 7. Comparison of OH and $O_2$ mass fraction along symmetric axis in subscale nozzle ($O/F = 5.5$, $T_w = 800$ K).

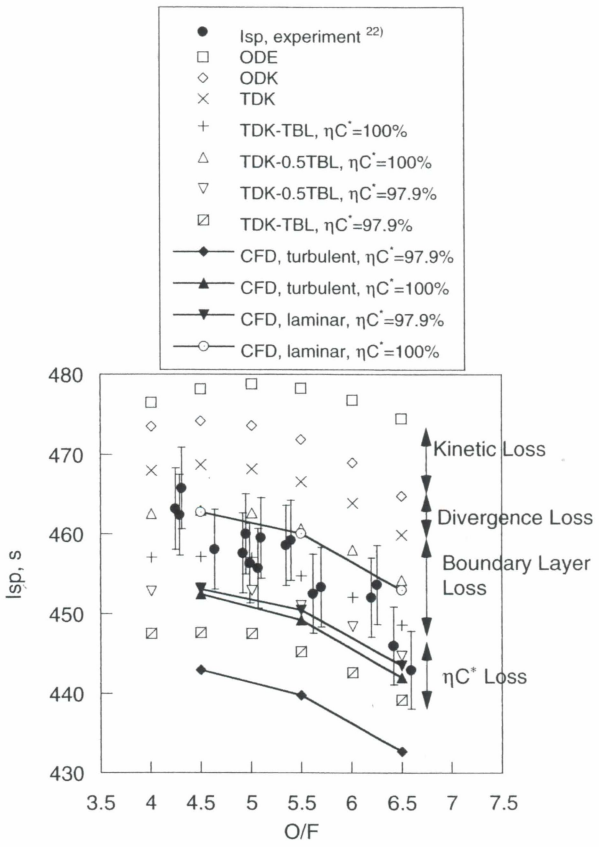


Fig. 8. Comparison of specific impulse in subscale nozzle.

of nozzle flow using methane as fuel[26] and the effect of the chemical reaction model on the nozzle flow seems small.

The comparison of $I_{sp}$ between TDK, CFD, and the experiments[22] is shown in Fig. 8. The $C^*$ efficiency ($\eta C^*$) of 0.979 is multiplied to the final $I_{sp}$ obtained from TDK and CFD. The kinetic loss (ODE-ODK) due to the chemical non-equilibrium, boundary layer loss (TDK-TBL), and divergence loss (ODK-TDK) are calculated by the TDK code. The TDK results show that the kinetic loss due to the chemical non-equilibrium becomes large as the mixture ratio increase. In the present case, the number of dissociated molecules increases and the kinetic loss due to chemical non-equilibrium becomes larger as the mixture ratio increases. This is because that the temperature inside the combustion chamber becomes higher as the mixture ratio increases. On the other hand, the divergence loss and boundary layer loss are insensitive to change in the mixture ratio. The divergence loss and boundary layer loss are not influenced by mixture ratio. However, the chemical non-equilibrium loss is influenced by the mixture ratio (Fig. 9). At low mixture ratio regions, the TDK results tend to disagree with the experiment and same trend can be found in the CFD results. The results for TDK with half the turbulence effect (TDK-0.5 TBL) agree well with laminar CFD. However, the discrepancy between the TDK (TDK-TBL) and the turbulent CFD is approximately 5 s. The specific impulse loss due to the boundary layer obtained by the TBL code is compared to that obtained by the more sophisticated BLIMP code[27] in Ref. 25). The boundary layer loss obtained by

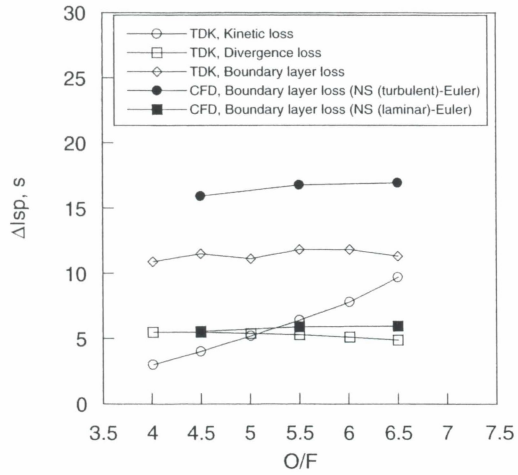


Fig. 9. Comparison of thrust loss in subscale nozzle.

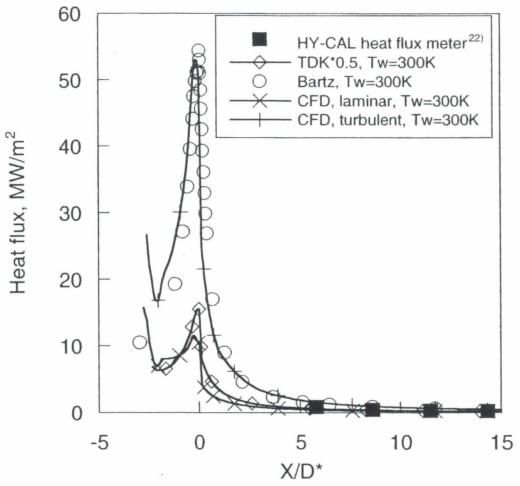


Fig. 10. Comparison of heat flux on wall in subscale nozzle ($O/F = 5.5$).

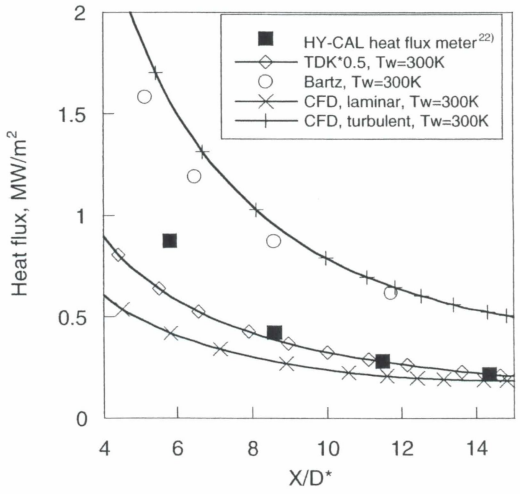


Fig. 11. Comparison of heat flux on wall in subscale nozzle ($O/F = 5.5$). Close-up of Fig. 10.

the BLIMP code at a throat Reynolds number of $4.7 \times 10^5$ is half the loss obtained by the TBL code, showing that the boundary layer is nearly laminar. These discussions agree well with the fact that the laminar CFD and TDK-0.5 TBL almost coincide. Therefore, CFD and TDK computations should be carried out assuming laminar boundary layer conditions.

The comparison of thrust loss between TDK and CFD is shown in Fig. 9. For CFD, the thrust loss between the inviscid flow condition (slip and adiabatic wall condition) and the viscous condition (laminar and turbulent condition) is shown. For the TDK simulations, the chemical non-equilibrium loss and the divergence loss are obtained by carrying out the inviscid flow computation, and the boundary layer loss is obtained by solving the boundary layer equations. Therefore, the same procedure between TDK and CFD is used to obtain the boundary layer loss. The turbulent CFD computations produce larger boundary layer loss (about 6 s) than the TDK result from Fig. 9. On the other hand, the laminar CFD computations produce about half the boundary layer loss compared to the TDK result.

The comparison of the heat flux on the wall is shown in Figs. 10 and 11. The experiment[22] shows the result obtained by using thin-film heat transfer gauges (denoted as HY-CAL in the figures after the name of the manufacturer). The measured heat flux is obtained at a wall temperature of 300–400 K. Although the heat flux obtained by CFD depends strongly on the minimum grid size near the wall, its convergence has been evaluated previously and the present grid is confirmed to have $y^+ < 1$ for the minimum width. The heat flux obtained by TDK is evaluated in half (0.5*TDK) as the measured heat flux in the subscale experiments agreed well with that of half the heat flux obtained by TDK. The fact that the $I_{sp}$ in TDK-0.5 TBL and the experiment agree well is consistent with the Reynolds analogy where heat flux is proportional to friction. The peak heat flux obtained by the laminar CFD is about 70% that of the TDK results. Its value becomes almost the same at the nozzle exit. However, the peak heat flux obtained by the turbulent CFD is three times that of the TDK results and becomes twice the TDK results at the nozzle exit. The turbulence model introduced from the inlet of the nozzle wall causes rapid heat flux distribution in CFD near $X/D^* = -2.5$. However, this has no effect on the peak heat flux which appears downstream. The heat flux derived from Bartz's equation[28] is also plotted in Figs. 10 and 11 and shows good agreement with the turbulent CFD results.

### 3.2. Results of fullscale nozzle

Figure 12 shows the comparison of $I_{sp}$ between TDK and turbulent CFD for the fullscale nozzle. The combustion efficiency is assumed to be 100%. The loss due to chemical non-equilibrium of TDK for the fullscale nozzle is 1–5 s and is about half the value of the subscale nozzle. The increased nozzle size leads to longer fluid residence time in the nozzle. This suggested that there is more time for dissociated atoms to recombine, resulting in increased kinetic efficiency. As previously shown in the subscale nozzle, $I_{sp}$ in CFD becomes 5 s less than TDK. The comparison of thrust loss between TDK and CFD is shown in Fig. 13. These results are similar to those in the subscale nozzle (Fig. 9). The

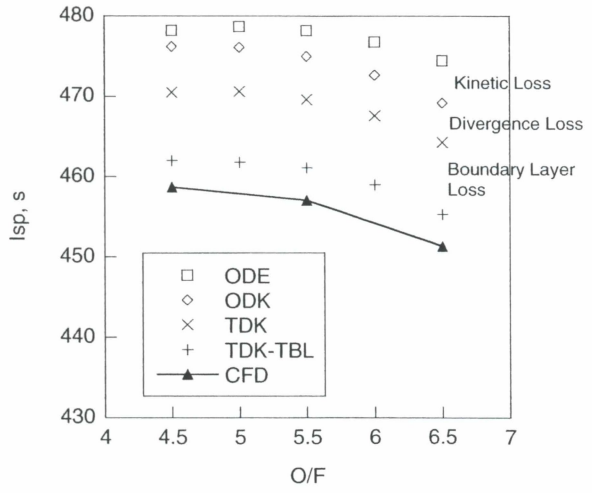


Fig. 12. Comparison of specific impulse in fullscale nozzle ($T_w$ = 800 K).

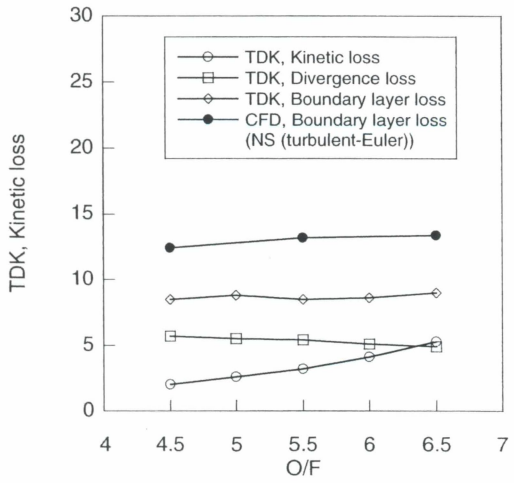


Fig. 13. Comparison of thrust loss in full nozzle.

boundary layer loss and the kinetic loss of TDK in the fullscale nozzle become smaller than in the subscale nozzle due to the increased nozzle size. The CFD computations produce a larger boundary layer loss of about 4 s than TDK.

Haidinger[8] estimated the effects of turbulences model compared with fullscale experimental data. He showed that the computed $I_{sp}$ using two equation models, such as the Menter shear-stress transport (SST) model, agrees well with the experimental data. He also showed that the Baldwin-Lomax Model (BLM) overpredicts the boundary layer loss by 3 s for adiabatic walls and by 6 s for cold walls. Our CFD computation was performed using BLM assuming that the wall temperature is constant ($T_w$ = 800 K), which is rather cold. The difference in $I_{sp}$ loss between CFD and TDK and between BLM and SST in Haidinger's paper is in approximate accord. This suggests that the turbulent boundary layer integral method (TBL) may reasonably predict $I_{sp}$, at least.

Heat flux distributions for a wall temperature of 800 K are shown in Fig. 14. The results obtained using the Bartz's equation[28] are also plotted in this figure for reference. Al-

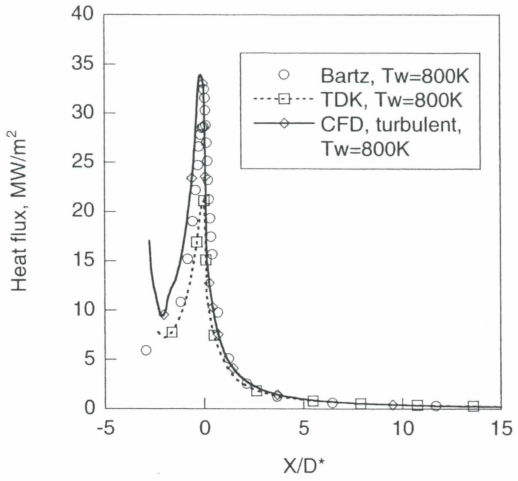


Fig. 14. Comparison of heat flux on wall in fullscale nozzle ($O/F$ = 5.5, $T_w$ = 800 K).

Table 2. Effects of grid resolution on $I_{sp}$.

| Grid | 1 | 2 | 3 | 4 | 5 | 6 | 7 |
|---|---|---|---|---|---|---|---|
| Jmax | 202 | 103 | 403 | 601 | 202 | 202 | 202 |
| Lmax | 77 | 77 | 77 | 77 | 51 | 101 | 201 |
| $I_{sp}$, s | 449.2 | 448.3 | 449.5 | 449.5 | 449.6 | 449.3 | 449.1 |

though all three results agree well in the supersonic region, there is large discrepancy near the nozzle throat. While the results of CFD and Bartz agree well, those for TDK are 40% less than the others. As reported previously, the Bartz equation reasonably predicts the heat flux near the throat area. Therefore, the CFD code can also predict the heat flux near the throat area. As seen in the subscale results, the turbulence model applied from the inlet of the nozzle wall again causes rapid heat flux distributions for the CFD results near $X/D^* = -2.5$.

### 3.3. Effects of grid resolution

To evaluate the effects of grid resolution on nozzle performance, the axial grid point (Jmax) and radial grid point (Lmax) were varied as listed in Table 2. The simulations were carried out for the subescale nozzle. The other simulation conditions are listed in Table 1. The mixture ratio is set to 5.5 and the flow is assumed to be turbulent. The wall temperature is set to 800 K, the minimum grid size is set to 0.1 μm, and 9 points (Kmax) are distributed in the circumferential direction. The obtained $I_{sp}$ is shown in Table 2, where the combustion efficiency is set to 100%. In Table 2, grid 1 is the same grid as used in section 3.1, grids 2–4 are used to investigate the effects of Jmax, and grids 5–7 are used to investigate the effects of Lmax. As shown in this table, the effects of Jmax and Lmax are within 1 s of $I_{sp}$ compared to the results obtained from grid 1. Therefore, the effects of grid resolutions on the $I_{sp}$ are small.

## 4. Conclusions

Numerical investigations on a bell nozzle with 10 tons of thrust, for which there are experimental data, were per-

formed for the viscous reactive flow with hydrogen/oxygen mixtures. The conclusions are as follows:

(1) The present CFD code accurately predicts $I_{sp}$ and heat flux distributions compared to the TDK data and experimental data. In particular, the turbulent peak heat flux can be predicted by the present CFD code.

(2) For the subscale nozzle:

- The boundary layer along the wall should be laminar rather than turbulent because the throat Reynolds number is within its transition region. This assumption can be proved because the calculated $I_{sp}$ and heat flux in the laminar flow agree well with the experimental results.

(3) For the fullscale nozzle:

- The $I_{sp}$ trend for the fullscale nozzle is similar to that for the subscale nozzle. The $I_{sp}$ in CFD was 5 s lower than the TDK results.
- The peak heat flux in TDK is smaller than that obtained by the Baltz equations. However, CFD showed good agreement with the peak heat flux obtained by the Baltz equations.

(4) The grid resolution turned out to be insensitive to $I_{sp}$ performance and within 1 s of difference.

## Acknowledgments

This research was carried out in collaboration with the Center for Planning and Information Systems at ISAS/JAXA.

## References

1) Gordon, S. and McBride, J. B.: Computer Program for Calculation of Complex Chemical Equilibrium Compositions, Rocket Performance, Incident and Reflected Shocks, and Chapman-Jouguet Detonations, NASA SP-273, 1971.
2) Nakahashi, K., Miyajima, H., Kisara, K. and Moro, A.: Prediction Method of Rocket Nozzle Performance, Technical Report of National Aerospace Laboratory NAL TR-771, 1983 (in Japanese).
3) Wang, T. S. and Chen, Y. S.: Unified Navier-Stokes Flowfield and Performance Analysis of Liquid Rocket Engines, *J. Propul. Power*, **9** (1993), pp. 678–685.
4) Wang, T. S. and Loung, V.: Hot-Gas-Side and Coolant-Side Heat Transfer in Liquid Rocket Engine Combusters, *J. Thermophys. Heat Transfer*, **8** (1994), pp. 524–530.
5) Wang, T. S.: Multidimentional Unstructured-Grid Liquid Rocket Engine Nozzle Performance and Heat Transfer Analysis, AIAA Paper 2004-4016, 2004.
6) Hagemann, G., Kruelle, G. and Hannemann, K.: Numerical Flowfield Analysis of the Next Generation Vulcan Nozzle, AIAA Paper 95-2782, 1995.
7) Yang, R. J.: Assessment of Turbulence and Chemistry Models for Film-Cooled Nozzle Flows, *J. Thermophys. Heat Transfer*, **10** (1996), pp. 284–289.
8) Haidinger, F. A.: Influence of Turbulence Modeling on the Performance Prediction for Rocket Engine Nozzles, *J. Propul. Power*, **15** (1999), pp. 523–529.
9) Takahashi, M., Ueda, S., Tomita, T., Takahashi, M., Aoki, K. and Tamura, H.: Transient Flow Simulation of a Compressed Truncated Perfect Nozzle, AIAA Paper 2001-3681, 2001.
10) Shimizu, T., Miyajima, H. and Kodera, M.: Numerical Study of Restricted Shock Separation in a Compressed Trancated Perfect Nozzle, *AIAA J.*, **44** (2006), pp. 576–584.
11) Fujii, K.: Practical Applications of New LU-ADI Scheme for the Three-Dimensional Navier-Stokes Computation of Transonic Viscous Flows, AIAA Paper 86-0513, 1986.
12) Wada, Y. and Liou, M.-S.: A Flux Splitting Scheme with High-Resolution and Robustness for Discontinuities, AIAA Paper 94-0083, 1994.
13) Shuen, J. S.: Upwind Differencing and LU Factorization for Chemical Non-equilibrium Navier-Stokes Equations, *J. Comput. Phys.*, **99** (1992), pp. 233–250.
14) Petersen, E. L. and Hanson, R. K.: Reduced Kinetics Mechanisms for Ram Accelerator Combustion, *J. Propul. Power*, **15** (1999), pp. 591–600.
15) Eto, K., Tsuboi, N. and Hayashi, A. K.: Numerical Study on Three-Dimensional C-J Detonation Waves: Detailed Propagating Mechanism and Existence of OH Radical, Proceedings of the Combustion Institute 30, 2004, pp. 1907–1913.
16) Fujii, K.: Unified Zonal Method Based on the Fortified Solution Algorithm, *J. Comput. Phys.*, **118** (1995), pp. 92–108.
17) Baldwin, B. S. and Lomax, H.: Thin Layer Approximation and Algebraic Model for Separated Turbulent Flows, AIAA Paper 78-257, 1978.
18) Back, L. H., Massier, P. F. and Cuffel, R. F.: Flow Phenomena and Convective Heat Transfer in a Conical Supersonic Nozzle, *J. Spacecraft Rockets*, **4** (1967), pp. 1040–1047.
19) Back, L. H., Cuffel, R. F. and Massier, P. F.: Laminarization of a Turbulent Boundary Layer in Nozzle Flow-Boundary Layer and Heat Transfer Measurements with Wall Cooling, *Trans. ASME J. Heat Transfer*, **92** (1970), pp. 333–344.
20) Kacynski, K. J., Pavli, A. J. and Smith, T. A.: Experimental Evaluation of Heat Transfer on a 1030 : 1 Area Ratio Rocket Nozzle, NASA TP 2726, 1987.
21) Smith, T. A.: Boundary Layer Development as a Function of Chamber Pressure in the NASA Lewis 1030 : 1 Area Ratio Rocket Nozzle, AIAA Paper 88-3301, 1988.
22) Miyajima, H., Moro, A., Kusaka, K., Nakahashi, K., Kuroda, Y., Kumagai, T., Kisaka, K., Kamata, M., Sato, M., Abe, N. and Katsuta, H.: Experimental Performance of a Small $LOXH_2$ Thrust Chamber with a High Area Ration Nozzle (I), Technical Report of National Aerospace Laboratory NAL TR-662, 1981 (in Japanese).
23) Kim, S. and VanOverbeke, T.: Calculations of Gaseous $H_2O_2$ Thruster, AIAA Paper 90-2490, 1990.
24) Yanagawa, K., Fujita, T., Miyajima, H. and Kishimoto, K.: High-Altitude Simulation Tests of the $LOX/LH_2$ Engine LE-5, *J. Propul. Power*, **1** (1985), pp. 180–186.
25) Schoenman, L.: Low-Thrust Isp Sensivity Study, NASA CR-165621, 1982.
26) Ito, T. and Miyajima, H.: Performance Characteristics of the Methene Fueled Rocket Nozzles, *J. Jpn. Soc. Aeronaut. Space Sci.*, **53** (2005), pp. 351–357.
27) Evans, R. M.: Boundary Layer Integral Matrix Procedure for JANNAF Rocket Engine Evaluation Methodology, BLIMP-J User's Manual, AEROTHERM UM-75-64 (NASA Contract NAS8-30930), July 1975.
28) Bartz, D. R.: A Simple Equation for Rapid Estimation of Rocket Nozzle Convective Heat Transfer Coefficients, *Jet Propul.*, **27** (1957), pp. 49–51.